

A PV generation data reconstruction method based on improved super-resolution generative adversarial network

Chengsheng Zhang, Zhenguo Shao, Changxu Jiang, Feixiong Chen^{*}

Fujian Smart Electrical Engineering Technology Research Center, College of Electrical Engineering and Automation, Fuzhou University, Fuzhou 350108, China

ARTICLE INFO

Keywords:

Super-resolution reconstruction
Generative adversarial network
PV generation data
Data analysis

ABSTRACT

With the growing penetration of solar photovoltaic (PV) generation, advanced data analysis methods have been applied to the smart grid operation. However, the low-temporal-resolution PV generation data limits the utilization of the data analysis methods, because the low-temporal-resolution PV generation data contains too little information. On the other hand, the existing data reconstruction methods are less than satisfactory in reconstructing high-temporal-resolution PV generation data from low-temporal-resolution data, since most of them cannot fully capture the characteristics of PV generation data. To address this issue, a PV generation data reconstruction method based on improved super-resolution generative adversarial network is proposed in this paper. First, a data-image construction method is proposed to encode the PV generation data into the so-called data-images. Furthermore, we develop a data-image super-resolution generative adversarial network (DISRGAN) model, and the data-images are used to train the DISRGAN model. Finally, based on the trained DISRGAN model, a general framework is developed to reconstruct high-temporal-resolution PV generation data from low-temporal-resolution data. Numerical experiments have been carried out based on PV generation data from the State Grid Corporation of China, to reconstruct the high-temporal-resolution data from low-temporal-resolution data. The results demonstrate the superior performance of the proposed framework compared with a series of state-of-the-art methods.

1. Introduction

The smart grid is an automated and advanced distributed energy delivery network with two-way flows of information and electricity [1]. With the development of the smart grid, the large-scale integration of solar photovoltaic (PV) generation into power system is an inevitable trend, which poses new challenges to the smart grid operation [2]. In this context, advanced data analysis methods are adopted to enhance the capability of the smart grid to integrate renewable energy. For example, various promising meta-heuristic algorithms have been proposed to analyze the characteristics of PV systems [3], and several optimization algorithms are utilized to seek the optimal solution of the energy storage system for smoothing the PV power fluctuations [4]. Besides, numerous data analysis methods are used for anomaly detection, forecasting, outage management, decision making, and so forth in the context of high penetration of PV generation [5].

Notably, high-quality data is essential for advanced data analysis methods [6]. The temporal resolution, which refers to the temporal frequency of data recorded, has a certain influence on the data quality.

The low-temporal-resolution data is short of detailed information because it is only the average or maximum value of each recording period [7]. An increase in temporal resolution will effectively improve the data quality. However, there are restrictions on obtaining high-temporal-resolution data in the smart grid. For example, the cost of devices and communication equipment for recording high-temporal-resolution data is high, and the data storage space is large [8]. Also, equipment failure and other reasons can easily result in losing the high-temporal-resolution data.

Consequently, it is of important signification to research the data reconstruction mechanism to obtain high-temporal-resolution data. However, most of the existing data reconstruction methods focus on recovering missing data [9–12]. There is a paucity of data reconstruction methods for reconstructing high-temporal-resolution data from low-temporal-resolution data, whose principle is essentially similar to that of the image super-resolution reconstruction. Generally, the image super-resolution reconstruction refers to recover a high-resolution (HR) image from a low-resolution (LR) degraded image [13]. Conventionally, the image super-resolution reconstruction methods can be mostly divided into two categories, including interpolation-based methods

^{*} Corresponding author.

E-mail address: feixiongchen@fzu.edu.cn (F. Chen).

<https://doi.org/10.1016/j.ijepes.2021.107129>

Received 8 December 2020; Received in revised form 1 March 2021; Accepted 17 April 2021

Available online 16 May 2021

0142-0615/© 2021 Elsevier Ltd. All rights reserved.

Nomenclature			
Indices and sets			
p	index of the data-image	$\mu_{D_p^{SR}}$	average values of D_p^{SR}
q	index of the high-temporal-resolution data point at the beginning of the sliding window	$\mu_{D_p^{HR}}$	average values of D_p^{HR}
t	index of the data point	$\sigma_{D_p^{SR}}$	standard deviations of D_p^{SR}
τ	index of the low-temporal-resolution data point corresponding to the sliding window	$\sigma_{D_p^{HR}}$	standard deviations of D_p^{HR}
D^{LR}	set of low-resolution data-images	$\sigma_{D_p^{SR} D_p^{HR}}$	covariance of D_p^{SR} and D_p^{HR}
D^{SR}	set of super-resolution data-images	$\varphi_{a,b}$	b -th feature map obtained by the VGG-19 model before the a -th pooling operation
D^{HR}	set of high-resolution data-images	λ	coefficient of the adversarial loss function
L	set of low-temporal-resolution PV generation data	Variables	
H	set of high-temporal-resolution PV generation data	L_τ, H_τ	low-temporal-resolution data point and its corresponding high-temporal-resolution data sequence
Parameters		x_{pR}, x_{pB}	pixel values in Red channel and Blue channel of the p -th image
R	pre-determined upscaling factors	x_p	image matrix of normalized RGB pixel value in the p -th image
r	square root of R	x_p'	original image matrix in the p -th image
s	side length of low-resolution data-image	x_p''	data reconstructed from the p -th super-resolution image
K	number of low-temporal-resolution data points within a period	\tilde{x}_t, x_t	values of reconstructed data and real data
m	number of data types	$G_{\theta_G}(\sim)$	outputs of the generator
P	total number of data-images	$D_{\theta_D}(\sim)$	outputs of the discriminator
w, h	width and height of the data-image	$p_G(D^{LR})$	probability distribution over the super-resolution data-images
T	total number of high-temporal-resolution PV generation data points	$p_H(D^{HR})$	probability distribution over the high-resolution data-images
x_{ij}	entry at i -th row of j -th column in the image matrix of the binary image	Functions	
X_{ij}	$r \times r$ matrix in the image matrix of the high-resolution binary image	l_G	generator loss function
G, D	generator and discriminator	l_D	discriminator loss function
θ_G, θ_D	weights and biases of generator and discriminator	$l_{content}$	content loss function
α	learning rate for training DISRGAN	l_{adv}	adversarial loss function
c	clipping parameter for training DISRGAN	l_{VGG}	VGG loss function
n	batch size for training DISRGAN		
n_{discr}	number of iterations for discriminator per generator		

[14,15], and regularization-based methods [16,17]. However, the conventional methods usually lose edge details and texture information, which causes the reconstructed image too smooth. With the development of deep learning in recent years, deep learning has been widely applied to the super-resolution reconstruction area. For example, the super-resolution convolutional neural network (SRCNN) [18] was proposed as the first deep learning application in the field of super-resolution reconstruction. Since then, a lot of convolutional neural network (CNN)-based network models have been proposed, e.g., dual-state recurrent network (DSRN) [19] residual-dense network (RDN) [20], cascading residual network (CARN) [21], and residual channel attention network (RCAN) [22]. In the field of smart grid, the Super Resolution Perception Net for State Estimation (SRPNSE) was proposed to improve data completeness in smart grid state estimation [23]. In [24], a Super Resolution Perception (SRP) based framework was presented to reconstruct high-temporal-resolution smart meter data effectively.

While CNN-based approaches have been successfully applied to the super-resolution reconstruction, they have limitations in two aspects: first, they rely on the context of small image regions, which contains too little information to recover details; second, they need a lot of training time [25]. Consequently, a super-resolution generative adversarial network (SRGAN) was proposed to promote perceptual quality and speed up training [26], which is a pioneering work of generative adversarial networks (GANs) in the field of super-resolution reconstruction. GANs, which were proposed for the first time in 2014 [27], are

also widely applied in the smart grid. For example, the GANs were used to reconstruct PMU data for smart grid dynamic security assessment [28], and a GAN-based approach was proposed for renewable energy scenario generation [29]. Moreover, a conditional improved Wasserstein GAN was developed for typical wind power scenario generation [30], and a semi-supervised GAN-based method was proposed for short-term wind power prediction [31]. In order to detect outages in some partially observable distribution systems, GANs were used to extract the complex spatiotemporal characteristics in an unsupervised manner [32].

Though the past several years has witnessed a burgeoning development of GANs, there are few studies on the electrical data super-resolution reconstruction mechanism. Li *et al* were the first to reconstruct the high-temporal-resolution electrical data using a SRGAN framework [8]. Compared with the traditional one-dimension data reconstruction method, the merits of the SRGAN framework are that data can be processed by using multiple channels, which means large amounts of data can be stored with nearly the same storage. But there is still room for improvement. For instance, the image construction method can be promoted to better reflect the data characteristics, and the pixel coordinates for storing data can be fixed in the image to enable the SRGAN model to learn the data characteristics more quickly. Moreover, the SRGAN model can be improved to reduce the training time to a large extent without decreasing the accuracy of data reconstruction.

In this paper, we propose a novel method for reconstructing high-temporal-resolution PV generation data from low-temporal-resolution

data. First, in order to capture the data characteristics, a sequence-to-point (seq2point) mapping algorithm with a sliding window is proposed, to map the high-temporal-resolution data sequence to the corresponding low-temporal-resolution data point. Furthermore, considering the periodicity of PV generation data, a data-image construction method based on seq2point mapping algorithm is proposed to encode PV generation data into data-images. After that, the data-image super-resolution generative adversarial network (DISRGAN) model is developed from the conventional SRGAN model, and trained by the obtained data-images. Finally, based on the data-image and the DISRGAN model, we propose a general framework that can be exploited for various types of PV generation data. In this way, the high-temporal-resolution data can be reconstructed from low-temporal-resolution data in terms of the proposed framework. The key contributions of the paper can be summarized as follows.

- 1) A seq2point mapping algorithm is proposed as one of the steps to construct data-images, to capture the PV generation data characteristics. By forming a sliding window over the high-temporal-resolution data, the high-temporal-resolution data sequence in the sliding window is mapped to the corresponding low-temporal-resolution data point, to establish the correlation between high-temporal-resolution and low-temporal-resolution PV generation data.
- 2) A novel data-image construction method is proposed to encode multi-dimensional data into the data-image, for converting data characteristics into image features. Different from the traditional methods that re-assemble data vectors into matrices without considering the periodicity of data, the proposed method encodes the PV generation data into fixed pixel coordinates of the data-image with considering the periodicity of PV generation data.
- 3) A data-image super-resolution generative adversarial network (DISRGAN) based on the conventional SRGAN model is developed. The Wasserstein distance is introduced into the DISRGAN model for improving the stability of training. Besides, the loss function is simplified to improve the learning efficiency and reconstruction accuracy of the DISRGAN model. The architecture is also improved to reduce the training time by modifying the activation functions and network layers.
- 4) A general framework consisting of the data-image and the DISRGAN model is proposed to reconstruct high-temporal-resolution PV generation data from low-temporal-resolution data. The superior performance of the proposed framework has been demonstrated through the comparisons with a series of conventional and state-of-the-art methods, which is indicated by the higher reconstruction accuracy.

The rest of this paper is organized as follows. In Section 2, we propose a data-image construction method to encode low-temporal-resolution and high-temporal-resolution PV generation data into the data-images, respectively. The DISRGAN model, which is used for data-image super-resolution reconstruction, is proposed in Section 3. Section 4 demonstrates the general framework for reconstructing high-temporal-resolution PV generation data from low-temporal-resolution data. In Section 5, we illustrate and evaluate the data reconstruction results. Section 6 concludes this paper.

2. Data-image

In this section, we first describe the definition of data-image briefly. Then, we introduce the seq2point mapping algorithm. Furthermore, based on the seq2point mapping algorithm, we illustrate how to mutually convert between the data-image and time-series data.

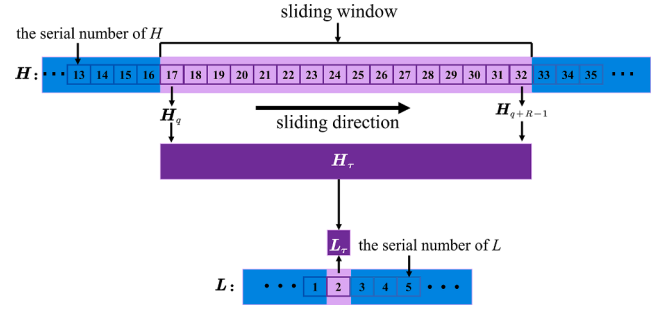


Fig. 1. Seq2point mapping algorithm ($R = 16$).

2.1. A brief description of data-image

A data-image is a 2-D pixel graphical representation of PV generation data, in which the pixel values represent the normalized PV generation data. In the data-image, the normalized PV generation data is stored in various channels as the pixel values. The low-temporal-resolution PV generation data is encoded into low-resolution data-images DI^{LR} while high-temporal-resolution data is encoded into high-resolution data-images DI^{HR} . Thereafter, DI^{LR} and DI^{HR} are utilized to train the DISRGAN model, to reconstruct high-temporal-resolution data, and the reconstructed high-temporal-resolution data is converted from super-resolution data-images DI^{SR} .

The pixel values of each color channel are expressed in the form of a two-dimensional image matrix whose size is the resolution of the data-image. We define that the resolution of low-resolution data-image DI^{LR} is $s \times s$, while both the high-resolution data-image DI^{HR} and super-resolution data-image DI^{SR} have the identical resolution of $(s \times r) \times (s \times r)$, where $r > 1$ is a positive integer and represents the square root of the pre-determined upscaling factors.

In order to calculate the data-image resolution, it is necessary to consider the periodicity of PV generation data. When data within a period is saved in a row of the image matrix, each row retains the data characteristics in every whole period, which helps convert data characteristics into image features completely. We define that the number of low-temporal-resolution data within one period is K . For the low-resolution data-image DI^{LR} whose resolution is $s \times s$, the number of entries in per row of image matrix must be greater than K , i.e., $s \geq K$. Similarly, for the high-resolution data-image DI^{HR} and the super-resolution data-image DI^{SR} , both of which have the identical resolution of $(s \times r) \times (s \times r)$, the number of entries in every r rows of image matrix must be greater than $K \times r$, i.e., $s \times r \geq K \times r$.

2.2. Seq2point mapping algorithm with sliding window

Since the resolution of low-resolution data-images, DI^{LR} , is increased with sub-pixel convolutional layers in the SRGAN-based model, and the pixel coordinates of high-resolution data-image DI^{HR} are corresponding to the ones of low-resolution data-image DI^{LR} [26]. Hence, it is necessary to map the time sequence of high-temporal-resolution data to the corresponding point of low-temporal-resolution data recorded at the same period, to establish the correlation between high-temporal-resolution and low-temporal-resolution PV generation data.

Algorithm 1 Seq2point mapping

Input: Low-temporal-resolution data (L), high-temporal-resolution data (H), pre-determined upscaling factors R , total number of high-temporal-resolution data T

Output: High-temporal-resolution data sequence H_τ and its corresponding low-temporal-resolution data point L_τ

```

1: for  $\tau = 1$  to  $T/R$  do
2:    $q = (\tau-1) \times R + 1$ 
3:    $L_\tau \leftarrow \{H_q, \dots, H_{q+R-1}\}$ 
4: end for
5:  $L_\tau \leftarrow H_\tau$ 

```

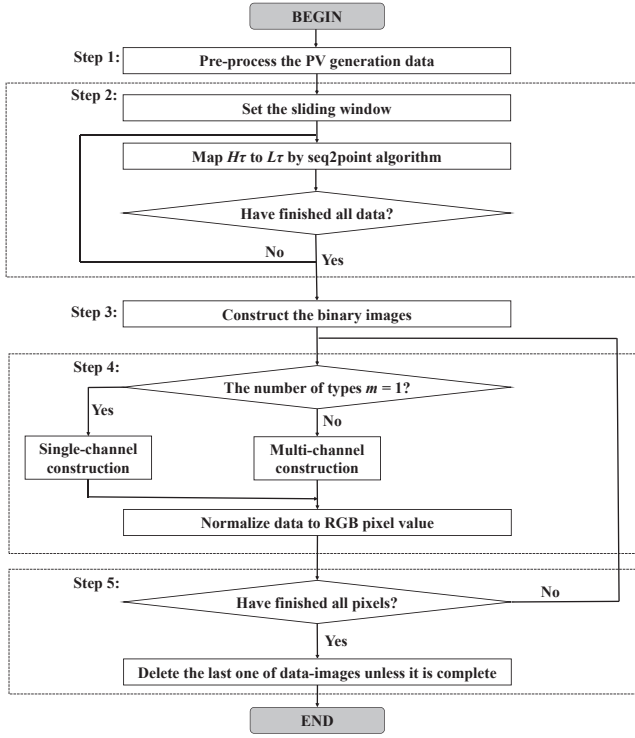


Fig. 2. Flowchart of the data-image construction method.

Therefore, a seq2point mapping algorithm with a sliding window is proposed as one of the steps to construct data-images, which is inspired by the seq2point learning method [33]. The process of the seq2point mapping algorithm (pre-determined upscaling factors $R = 16$) is shown in Fig. 1. A sliding window is formed over the set of high-temporal-resolution PV generation data H , and the window can slide over H to capture different portions of H . Both the length and the sliding step of the sliding window are set to R . Every time the window slides, the high-temporal-resolution data sequence in the sliding window H_r is mapped to the corresponding low-temporal-resolution data point L_r recorded at the same period. The seq2point mapping is summarized in Algorithm 1

2.3. Data-image construction method

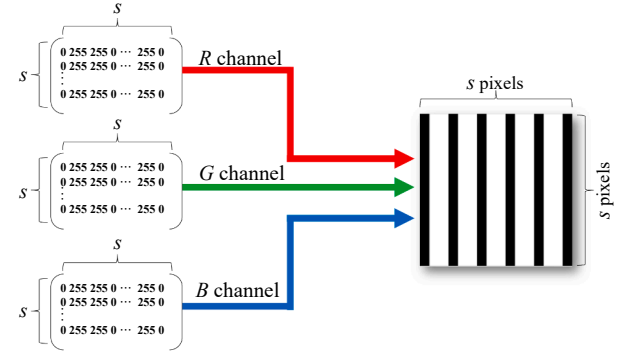
The flowchart of the data-image construction method is shown in Fig. 2. The steps are as follows.

Step 1: Pre-process the raw PV generation data. Once there is missing data at some positions, the linear interpolation method is adopted to fill up the data. It should be noted that the time continuity of pre-processed data should be ensured.

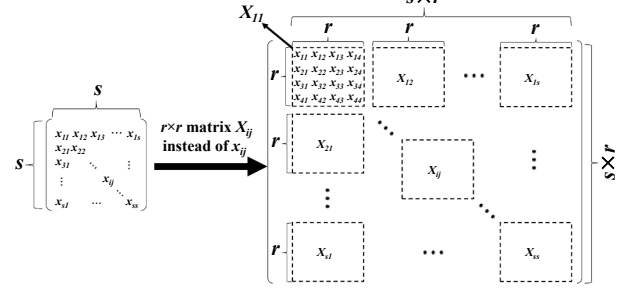
Step 2: Map the time sequence of high-temporal-resolution data H_r to the corresponding point of low-temporal-resolution data L_r . The seq2point mapping algorithm illustrated in Algorithm 1 is employed in this step.

Step 3: Construct the high-resolution and low-resolution binary images in terms of high-resolution and low-resolution data, respectively. As an example, when $r = 4$, the flowchart is shown in Fig. 3.

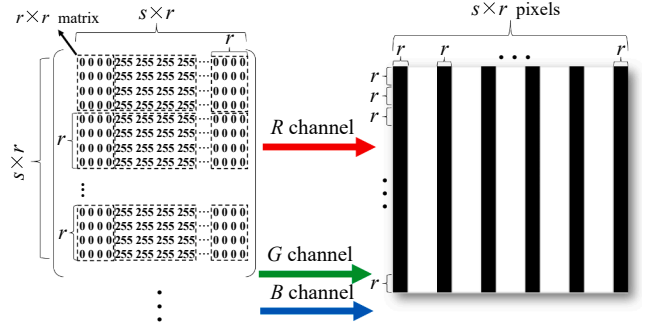
When the PV generation data is stored at the fixed pixel coordinates of the data-image, the conversion from data characteristics into image features is performed while maintaining the data characteristics. Consequently, to determine the pixel coordinates for data to be stored, it is necessary to construct the binary image as the basis for the data-image.



(a) Construction of the low-resolution binary image



(b) Correspondence between the low-resolution and the high-resolution binary image



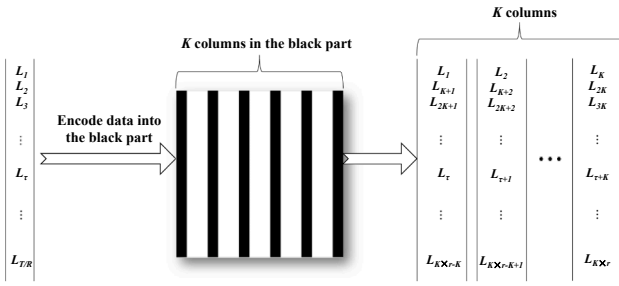
(c) Construction of the high-resolution binary image

Fig. 3. Flowchart of binary image construction ($r = 4$).

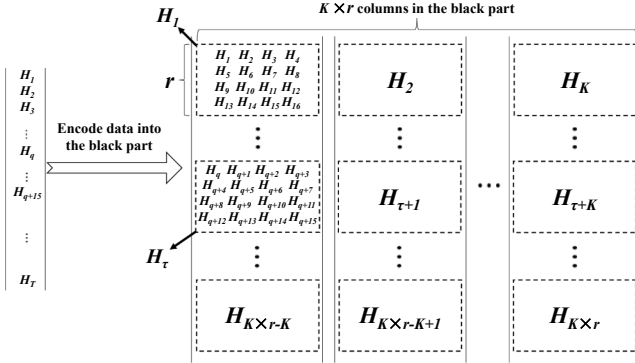
For low-resolution binary images, the x_{ij} represents the entry at i -th row of j -th column in the image matrix of each channel. If the pixel coordinate of x_{ij} is used for storing low-temporal-resolution PV generation data, then x_{ij} is set equal to 0, otherwise x_{ij} is set equal to 255. As shown in Fig. 3 (a), in the RGB color mode, the x_{ij} which is set equal to 0 is converted to the black part of the binary image, otherwise, x_{ij} is converted to the white part of the binary image.

After that, it is necessary to construct the high-resolution binary image based on the low-resolution binary image. The resolution of the low-resolution binary image is $s \times s$, while the resolution of high-resolution binary image is $(s \times r) \times (s \times r)$. The correspondence between the high-resolution and the low-resolution binary image is shown as Fig. 3 (b). Similarly, as shown in Fig. 3 (c), the entries in $r \times r$ matrix X_{ij} are all set equal to 0 when the X_{ij} is used to store high-temporal-resolution data, and it worth mentioning that the black part of high-resolution binary image corresponds to the black part of low-resolution binary image.

Step 4: According to the number of data types m , the construction method of the data-image can be divided into two categories, which are *single-channel construction* and *multi-channel construction*.



(a) Procedures of encoding data into one channel of the low-resolution binary image



(b) Procedures of encoding data into one channel of the high-resolution binary image

Fig. 4. Flowchart of encoding data into one channel of the binary image ($r = 4$).

Single-channel construction: If $m = 1$, encode the pre-processed PV generation data into the Red channel of the binary image. The process of encoding data into one channel of the binary image ($r = 4$) is shown in Fig. 4. For the low-resolution binary images, we encode low-temporal-resolution data L_τ into the black part of the Red channel in chronological order, as shown in Fig. 4 (a). And for the high-resolution binary images, we first realign high-temporal-resolution data H_τ into the matrices of size $r \times r$, then we also encode them into the black part of the Red channel, as shown in Fig. 4 (b).

Normalize data stored in the Red channel and convert it into the commonly used range of RGB pixel value, which is $[0, 255]$. The formula is shown as follows,

$$x_p = \frac{x'_p - \min(x'_p)}{\max(x'_p) - \min(x'_p)} \times 255 \quad (1)$$

where x'_p represents the original image matrix of the p -th image, x_p represents the image matrix of normalized RGB pixel value, $\max(x'_p)$ and $\min(x'_p)$ are the maximum and minimum of x'_p , respectively.

Furthermore, the pixel values in the Blue channel are calculated, so that the color textures of the data-image can reflect the data characteristics. The calculation formula of pixel values in the Blue channel is shown as follows,

$$x_{pB} = 255 - x_{pR} \quad (2)$$

where x_{pR} and x_{pB} represent the pixel values in Red channel and Blue channel of the p -th image, respectively.

Multi-channel construction: If $m \neq 1$, we encode the pre-processed data into the image matrix of different channels, including Red channel, Green channel, and Blue channel. However, the data-images with RGB

color mode have only three channels. Hence, when $m > 3$, we need to add extra $(m-3)$ channels to store the data.

The encoding process is the same as the encoding process in single-channel construction, but it should be mentioned that the Blue channel is used for storing other types of pre-processed data, so the pixel values in the Blue channel do not need to be calculated as formula (2).

Step 5: Delete the last one of constructed data-images unless the data can be completely encoded into the black part of the last data-image, because the incomplete data-image, whose black part is not encoded by data completely, would have a great impact on the reconstruction result.

2.4. Conversion from data-image to time-series data

Similarly, the data-image can also be converted to time-series data, and the steps are as follows.

Step 1: According to the category of the data-image construction method, identify which channels of data-image are used to store data. In the case of the single-channel construction, the data is only stored in the Red channel. As for the case of multi-channel construction, the data is stored in m channels of the data-images.

Step 2: For the single-channel construction, get all pixel values from the Red channel. De-normalize the pixel value x_p to the reconstructed data in terms of (3),

$$x''_p = \min(x'_p) + \frac{(\max(x'_p) - \min(x'_p)) \times x_p}{255} \quad (3)$$

where x''_p represents the reconstructed data from the p -th reconstructed image. For the multi-channel construction, the same conversion method is applied to the data stored in other $(m-1)$ channels.

Step 3: According to the pixel coordinates for storing data in the data-image shown in Fig. 4, arrange the de-normalized data from all data-images in chronological order.

3. Data-image super-resolution generative adversarial network

In this section, we introduce the DISRGAN model and how it is used for super-resolution data-image reconstruction. We firstly provide an overview of DISRGAN, then we illustrate the loss function as well as the structure of the DISRGAN model.

3.1. DISRGAN overview

As an emerging deep learning model, the SRGAN [26] has demonstrated state-of-the-art performance in a vast number of tasks. In this paper, the DISRGAN model is developed from the conventional SRGAN model by modifying its architecture and loss function.

DISRGAN is implemented with two deep neural networks, namely, *generator* and *discriminator*. Specifically, the generator is to generate super-resolution data-images D_I^{SR} whose probability distribution $P_G(D_I^{SR})$ follows the probability distribution over the high-resolution data-images $P_H(D_I^{HR})$, while the discriminator is to distinguish between the generated super-resolution data-images D_I^{SR} and the high-resolution data-images D_I^{HR} .

Generator: During the training process, the generator aims to minimize the probability of the discriminator correctly identifying its output. It means that the generator, which takes low-resolution data-images D_I^{LR} as the input, is trained to render its output super-resolution data-image D_I^{SR} indistinguishable from high-resolution data-image D_I^{HR} finally.

Discriminator: The discriminator, whose inputs are super-resolution data-image D_I^{SR} and high-resolution data-image D_I^{HR} , is trained simultaneously with the generator. The output of the discriminator is a

number, which is the classification score to reason whether the input is super-resolution data-image DI^{SR} or high-resolution data-image DI^{HR} . The discriminator aims to *maximize* the probability of correctly identifying the source of the input samples. It means that the discriminator is trained to render super-resolution data-image DI^{SR} distinguishable from high-resolution data-image DI^{HR} finally.

The training process can be divided into two steps: updating the discriminator with fixed generator parameters and updating the generator with fixed discriminator parameters. The interaction between the two deep neural networks can be modeled as a game-theoretic two-player nested min-max optimization,

$$\min_{\theta_G} \max_{\theta_D} E_{DI^{HR} \sim P_H(DI^{HR})} [\log(D_{\theta_D}(DI^{HR}))] + E_{DI^{LR} \sim P_G(DI^{LR})} [\log(1 - D_{\theta_D}(G_{\theta_G}(DI^{LR})))] \quad (4)$$

where $G_{\theta_G}(DI^{LR})$ denotes super-resolution data-images, $D_{\theta_D}(\sim)$ represents the output of the discriminator network, θ_G and θ_D represent network parameters in generator and discriminator respectively.

Compared with the conventional SRGAN model, we introduce the Wasserstein distance into the DISRGAN model for improving the stability of training. Besides, we modify the loss function of the conventional SRGAN model by removing the VGG loss to improve the learning efficiency and reconstruction accuracy of the DISRGAN model. The architecture is also modified to reduce the training time by modifying the activation functions and network layers. The modifications are described in Sections 3.2 and 3.3.

3.2. Loss function

For DISRGAN, the network parameters θ_G denote the weights and biases of the generator while θ_D denote those of the discriminator. Both θ_G and θ_D are updated by the loss functions, including *objective function*,

generator loss function, *discriminator loss function*.

Objective function: the traditional distance between $P_G(DI^{LR})$ and $P_H(DI^{HR})$ was measured by JS divergences, which have some limitations, such as gradient disappearance, gradient instability, and insufficient diversity of generated samples. The introduction of *Wasserstein* distance can effectively improve the stability of training [34]. By introducing Wasserstein distance into the model, the game-theoretic two-player nested min-max optimization shown in (4) can be reformulated as follows,

$$\min_{\theta_G} \max_{\theta_D} \sum_{p=1}^P D_{\theta_D}(DI^{HR}) - \sum_{p=1}^P D_{\theta_D}(G_{\theta_G}(DI^{LR})) \quad (5)$$

where P is the total number of images.

Generator loss function: The generator loss function, also known as the perceptual loss function, plays a vital role in the performance of the generator. The perceptual loss function is divided into two parts: content loss and adversarial loss.

The conventional content loss function includes pixel-wise MSE loss and VGG loss, in which the main purpose of VGG loss is to improve the quality of super-resolution images in terms of human perception. To calculate the VGG loss function, the VGG-19 model is introduced [26]. The VGG loss function is calculated as,

$$l_{VGG} = \frac{1}{R^2} \sum_{p=1}^P \sum_{w=1}^{\sqrt{R_s}} \sum_{h=1}^{\sqrt{R_s}} (\varphi_{a,b}(DI_p^{HR})_{w,h} - \varphi_{a,b}(G_{\theta_G}(DI_p^{LR}))_{w,h})^2 \quad (6)$$

where w and h are respectively the width and height of the image pixel, $\varphi_{a,b}$ is the b -th feature map obtained by the VGG-19 model before the a -th pooling operation.

It can be observed that VGG loss is to improve the identification accuracy from the perspective of visual observation. However, it worth

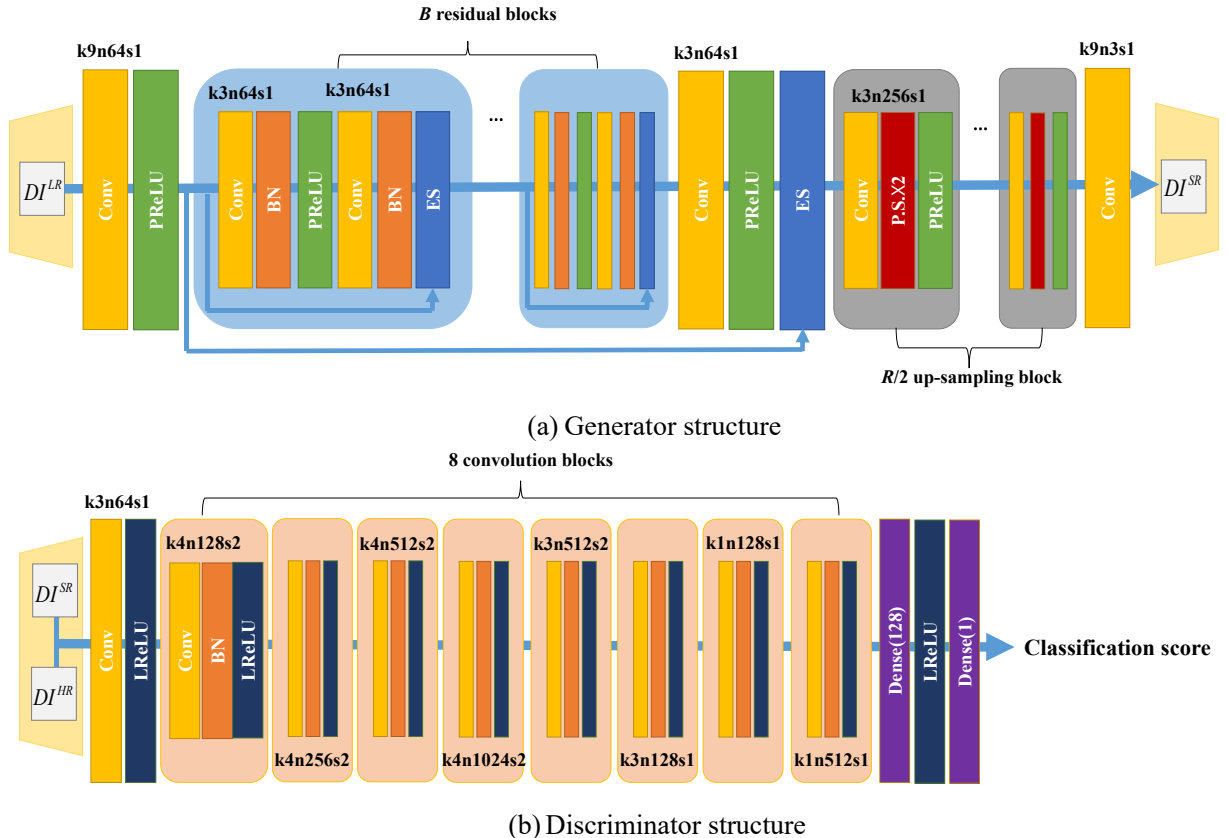


Fig. 5. Structure of DISRGAN.

mentioning that the proposed data-image is simpler in color texture and high-resolution details compared with images in the field of computer vision. On the other hand, for the data-image, VGG loss will reduce the accuracy of data reconstruction because it can simply improve the quality of images for visual observation, without considering the reconstruction effect of the data. Also, it takes time for the VGG-19 model to extract the features from data-images, which decreases the learning efficiency of the DISRGAN model. Accordingly, the VGG loss function does not apply to the reconstruction method proposed in this paper and it is removed from the proposed DISRGAN model. Therefore, the content loss is considered as the MSE loss, for the reason that it is helpful to improve the learning efficiency and reconstruction accuracy of the DISRGAN model. Therefore, the content loss function is formulated as follows,

$$l_{content} = \frac{1}{R^2 s^2} \sum_{p=1}^P \sum_{w=1}^{\sqrt{R}s} \sum_{h=1}^{\sqrt{R}s} \left((DI_p^{HR})_{w,h} - G_{\theta_G}(DI_p^{LR})_{w,h} \right)^2 \quad (7)$$

The generator adversarial loss, which helps the generator produce better details and more plausible colors, is shown as follows,

$$l_{adv} = -\lambda \sum_{p=1}^P D_{\theta_D}(G_{\theta_G}(DI_p^{LR})) \quad (8)$$

where the coefficient of adversarial loss $\lambda = 1 \times 10^{-3}$.

In summary, the perceptual loss function can be calculated as,

$$l_G = l_{content} + l_{adv} \quad (9)$$

Discriminator loss function: Compared with the generator loss function consisting of several loss functions, the discriminator loss function is only the adversarial loss, which is shown as follows,

$$l_D = \sum_{p=1}^P D_{\theta_D}(G_{\theta_G}(DI_p^{LR})) - \sum_{p=1}^P D_{\theta_D}(DI_p^{HR}) \quad (10)$$

As mentioned before, the training process of DISRGAN is detailed in Algorithm 2.

Algorithm 2 DISRGAN Training Process

Input: Learning rate α , clipping parameter c , batch size n , number of iterations for discriminator n_{discr}

Output: Super-resolution data-image DI^{SR}

Initialize: network parameters in generator θ_G and discriminator θ_D

1: **for** the number of training epochs **do**

2: **for** $i = 0, \dots, n_{discr}$ **do**

 # Update discriminator parameter

3: Sample batch from high-resolution data-images:

4: $\{DI^{HR(i)}\}_{i=1}^n \sim p_H(DI^{HR})$

5: Sample batch from low-resolution data-images:

6: $\{DI^{LR(i)}\}_{i=1}^n \sim p_G(DI^{LR})$

7: Update discriminator nets using gradient descent:

8: $g_{\theta_D} \leftarrow \nabla_{\theta_D} \left[-\frac{1}{n} \sum_{i=1}^n D_{\theta_D}(DI^{HR(i)}) + \frac{1}{n} \sum_{i=1}^n D_{\theta_D}(G_{\theta_G}(DI^{LR(i)})) \right]$

9: $\theta_D \leftarrow \theta_D - \alpha \cdot \text{Adam}(\theta_D, g_{\theta_D})$

10: $\theta_D \leftarrow \text{clip}(\theta_D, -c, c)$

11: **end for**

 # Update generator parameter

12: Update generator nets using gradient descent:

13: $g_{\theta_G} \leftarrow \nabla_{\theta_G} \frac{1}{n} \sum_{i=1}^n \left[-\lambda \cdot D_{\theta_D}(G_{\theta_G}(DI^{LR(i)})) + \frac{1}{R^2 s^2} \sum_{w=1}^{\sqrt{R}s} \sum_{h=1}^{\sqrt{R}s} \left((DI_{w,h}^{HR(i)} - G_{\theta_G}(DI_{w,h}^{LR(i)})) \right)^2 \right]$

14: $\theta_G \leftarrow \theta_G - \alpha \cdot \text{Adam}(\theta_G, g_{\theta_G})$

15: **end for**

3.3. Structure

Given the difficulty in training deep neural networks, the Deep Residual Network (DRN) is applied to the generator structure [35]. The generator structure is shown as Fig. 5 (a), which consists of residual

blocks, up-sampling blocks, convolutional layers, activation function layers, and an element-wise sum (ES) layer. Herein, “Conv”, “BN” and “ES” mean the convolution layer, the batch normalization layer, and the element-wise sum layer, respectively. Comparing with the conventional SRGAN, the number of identical residual blocks is set to 5 ($B = 5$) in our generator structure. The up-sampling block structure adopts the pixel-shuffle layer [36] so that it can magnify the resolution by 2 times. Consequently, there are $(R/2)$ up-sampling blocks in the generator structure. All activation functions are set to ParametricReLU [37] for making the calculation efficient. The numbers after symbols k , n and s represent kernel size, the number of filters and stride size, respectively. For example, k9n64s1 refers to the convolution layer containing 64 filters, of which the spatial size is 9 and stride is 1.

On the other hand, the Deep Convolutional Network (DCN) is used as the discriminator shown in Fig. 5 (b), which has brilliant performance in classification [38]. The convolution block includes a convolutional layer, a BN layer, and an activation function layer. To accelerate the convergence speed of the model and improve the accuracy of model recognition, dense layers are utilized at the tail of the discriminator. All activation functions here are regarded as leakyReLU [39], which can improve the recognition accuracy of the discriminator without using a pooling operation.

4. General framework

Based on the data-image and DISRGAN model discussed above, a general framework is proposed to fully capture the data characteristics and exploit the data-image features, to reconstruct high-temporal-resolution PV generation data from low-temporal-resolution data, as shown in Fig. 6. According to Fig. 6, there are main two steps for data reconstruction, i.e., the DISRGAN model training and data reconstruction.

4.1. DISRGAN model training

As shown by the solid line in Fig. 6, we encode the prior low-

temporal-resolution PV generation data into low-resolution data-images, which are the inputs of the generator. In terms of the low-resolution data-images, the generator will generate super-resolution data-images, which are imported to the discriminator. On the other hand, we encode the prior high-temporal-resolution PV generation data

into high-resolution data-images, which are also imported to the discriminator. It is observed that the high-resolution data-image and the generated super-resolution data-image have the same resolution. After that, the discriminator calculates the classification score to reason whether the input is the high-resolution data-image or the super-resolution data-image.

Then, according to Algorithm 2 demonstrated in Section 3.2, the generator and discriminator will be trained by constantly updating and fixing network parameters of each other.

After the number of training epochs reaches the preset value or the loss function converges, the probability distribution over generated super-resolution data-images is similar to that over high-resolution data-images, which means the generator can generate accurate complete samples. Up to now, the trained generator could be used for reconstructing high-temporal-resolution PV generation data from low-temporal-resolution data, whose procedure is shown by the dotted line in Fig. 6.

4.2. Reconstructing data by the trained generator

As shown by the dotted line in Fig. 6, the low-temporal-resolution data is encoded into low-resolution data-images firstly. Then, they will be imported into the generator, and the generator will produce the reconstructed super-resolution data-images. In the end, the reconstructed high-temporal-resolution data can be restored from reconstructed super-resolution data-images. In this way, the high-temporal-resolution PV generation data is reconstructed from the low-temporal-resolution data.

5. Numerical test

In this section, we first illustrate some statistical indicators. Then, we describe how to preprocess data and demonstrate details in model training. Furthermore, we verify the effectiveness of the proposed framework in two cases. The two cases are carried out in this section:

- Case 1: In this case, we compare the performance of the *data-image* construction method with the existing *electrical image construction* method, and the DISRGAN model is used as the numerical test model

to reconstruct high-temporal-resolution PV generation data from low-temporal-resolution data. In terms of the reconstructed images and data, we evaluate the accuracy of *data-image* and *electrical image* construction methods in data and image reconstruction.

- Case 2: In this case, we compare the performance of the *DISRGAN model* with the *existing SRGAN model*, and we use the *data-image* construction method to encode data into images. Similarly, in terms of the reconstructed data, we evaluate the accuracy of the proposed *DISRGAN model* and the *existing SRGAN model* in data reconstruction. Moreover, we compare the model training time between the above two models.

We test our framework based on PV generation data sets from the State Grid Corporation of China. There are a total of 66,720 data groups in the dataset which cover a period from April 1, 2016 to April 30, 2018. The temporal resolution of data is 15 min.

All numerical tests, which run on a 64-bit desktop with an Intel Core i5 CPU of 2.4-GHz and 16-GB RAM, are coded in Python 3.6.2. We implement the DISRGAN model with PyTorch [40] on the PC with an Nvidia GeForce RTX 2060 GPU.

5.1. Statistical indicator

Some statistical indicators will be employed in this paper to evaluate the reconstruction results.

The Peak signal-to-noise rate (PSNR) [41] and the Structural Similarity (SSIM) [42] are extensively used in the computer vision area for evaluating the effectiveness of super-resolution reconstruction. In this paper, PSNR and SSIM are adopted to measure the quality of reconstructed images.

The PSNR measures the quality of super-resolution data-images by calculating the difference between the pixel values of super-resolution data-images Dl^{SR} and the corresponding high-resolution data-images Dl^{HR} . The calculation formula of PSNR is shown as follows,

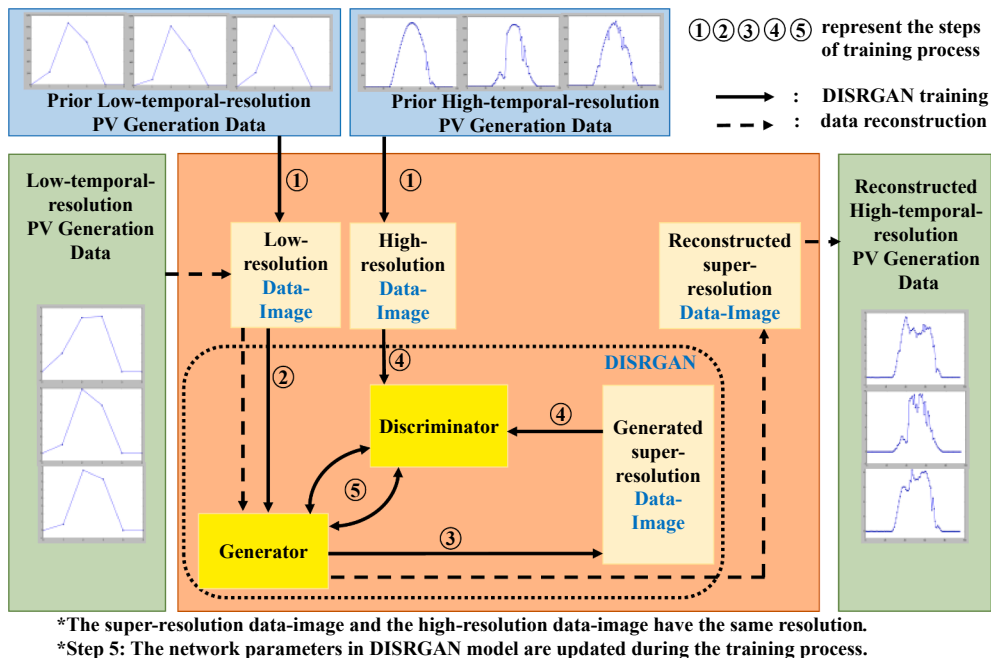


Fig. 6. The general framework for PV generation data reconstruction.

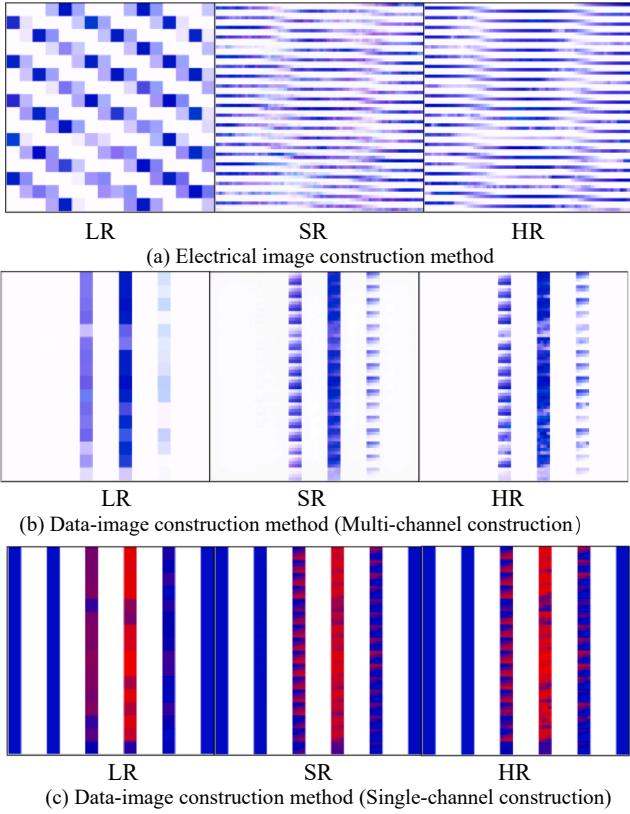


Fig. 7. Image reconstruction results of different image construction methods. Acronyms: LR → Low-resolution image, SR → Super-resolution image, HR → High-resolution image.

$$PSNR(DI^{SR}, DI^{HR}) = \frac{255^2}{10 \lg \frac{1}{s^2} \sum_{w,h} (DI_{w,h}^{SR} - DI_{w,h}^{HR})^2} \quad (11)$$

The range of PSNR is $[0, +\infty)$.

In addition, SSIM is calculated as follows,

$$SSIM(DI_p^{SR}, DI_p^{HR}) = \frac{(2\mu_{DI_p^{SR}}\mu_{DI_p^{HR}} + k_1)(2\sigma_{DI_p^{SR}DI_p^{HR}} + k_2)}{(\mu_{DI_p^{SR}}^2 + \mu_{DI_p^{HR}}^2 + k_1)(\sigma_{DI_p^{SR}}^2 + \sigma_{DI_p^{HR}}^2 + k_2)} \quad (12)$$

where $\mu_{DI_p^{SR}}$ and $\mu_{DI_p^{HR}}$ respectively represent the averages of DI_p^{SR} and DI_p^{HR} while $\sigma_{DI_p^{SR}}$ and $\sigma_{DI_p^{HR}}$ respectively are the standard deviations of DI_p^{SR} and DI_p^{HR} , $\sigma_{DI_p^{SR}DI_p^{HR}}$ is the covariance of DI_p^{SR} and DI_p^{HR} , k_1 and k_2 are constants, where $k_1 = 0.01 \times 255$, and $k_2 = 0.03 \times 255$. The higher the quality of the reconstructed image, the greater both the PSNR and SSIM values will be.

Moreover, some statistical indicators are used to compare real PV generation data and reconstructed PV generation data. The statistical indicators include the mean, median, standard deviation (St.dev), skewness and kurtosis. The accurate statistical indicators of the real data are used as benchmarks for evaluating the reconstructed data.

Besides, the Root Mean Squared Error (RMSE), the Mean Absolute Error (MAE) and the coefficient of determination (R^2) are utilized to further evaluate the accuracy of the reconstructed PV generation data under different cases. The RMSE, MAE, and R^2 are defined as,

Table 1

Evaluation results of image reconstruction accuracy of different image construction methods.

image construction methods	PSNR/dB	SSIM
electrical image construction method in [8]	17.61	0.86
multi-channel construction method	26.63	0.94
single-channel construction method ¹	31.20	0.98
single-channel construction method ²	30.87	0.97

Data-image construction¹ takes ‘irradiance’ data to be reconstructed;

Data-image construction² takes ‘PV power’ data to be reconstructed.

$$RMSE = \sqrt{\frac{1}{T} \sum_{t=1}^T (\hat{x}_t - x_t)^2} \quad (13)$$

$$MAE = \frac{1}{T} \sum_{t=1}^T |\hat{x}_t - x_t| \quad (14)$$

$$R^2 = \frac{\sum_{t=1}^T (\hat{x}_t - \bar{x})^2}{\sum_{t=1}^T (x_t - \bar{x})^2} \quad (15)$$

where T is the total number of reconstructed data, \hat{x}_t , x_t and \bar{x} are reconstructed data values, real data values, and the mean value of real data, respectively. The smaller RMSE and MAE, the better the effect of data reconstruction will be, and R^2 closer to one indicates that the reconstructed data can correctly represent the real samples.

5.2. Data preprocessing and model training

Before the model training, it is necessary to preprocess the data. The data characteristics within every 24 h are similar, so we define the period of the PV power generation data sets as 24 h. The temporal resolution of low-temporal-resolution and high-temporal-resolution data are 4 h and 15 min, respectively. Consequently, in this test, $K = 24/4 = 6$.

We set the side length of the low-resolution data-image as $s = 16$ while the side length of the high-resolution data-image can be obtained as $(s \times r) = 64$. Accordingly, the number of hours that can be stored in a data-image is $24 \times s = 384$.

In this study, the number of training batches is set as the number of pictures in the training set, and the number of training epochs is set to 2500. Meanwhile, the implementation was done under Adam optimizer, and the initial learning rate is 0.0001. Moreover, let the learning rate be 1/10 of the initial learning rate after every 500 epochs.

5.3. Comparison between different image construction methods

In this subsection, the data sets of irradiance and PV power are encoded into images to compare the proposed data-image construction method with the electrical image construction method in [8], respectively. The amount of data used by different image construction methods is almost the same. For the electrical image construction method, the training set and test set respectively contain 57,344 and 8192 groups of data. In this way, we can construct $(57344 + 8192)/(s \times r)^2 = 16$ electrical images, among which 14 electrical images are training sets and the other 2 electrical images are test sets. In comparison, the training set and test set respectively contain 58,368 and 7680 groups of data for the data-image construction method. In terms of the proposed data-image method, we can construct $(58368 + 7680)/(K \times R \times s) = 43$ data-images, among which 38 data-images are training sets and the other 5 data-images are test sets.

The DISRGAN model is used as the numerical test model in this subsection to reconstruct high-temporal-resolution PV generation data

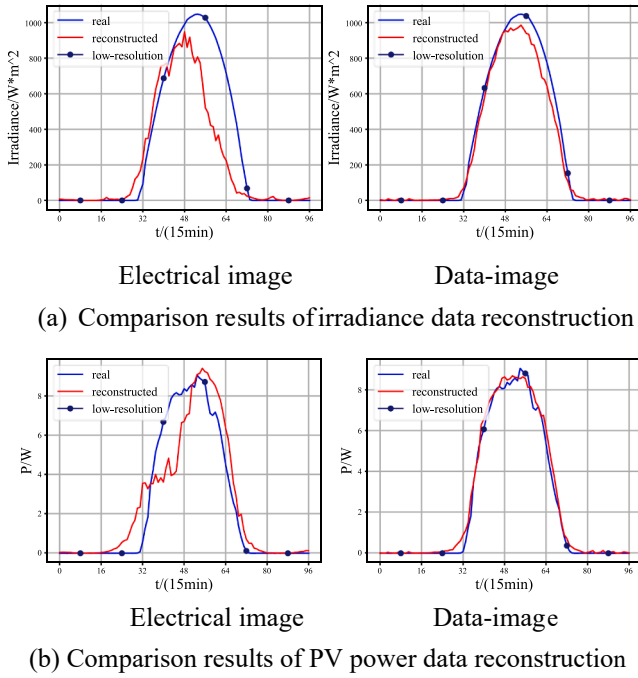


Fig. 8. Data reconstruction curves of different image construction methods.

Table 2

Evaluation results of data reconstruction accuracy of different image construction methods.

Statistic	Data type	Real	Method ¹	Method ²	Method ³
MAE	Irradiance		102.69	55.26	50.33
	PV power		0.908	0.467	0.452
RMSE	Irradiance		182.65	110.15	94.94
	PV power		1.618	0.919	0.851
R^2	Irradiance		0.74	0.91	0.93
	PV power		0.76	0.92	0.93
Mean	Irradiance	247.20	227.27	246.33	248.48
	PV power	2.299	2.187	2.270	2.302
Median	Irradiance	0.00	32.37	18.41	26.36
	PV power	-0.019	0.258	0.127	0.185
St.dev	Irradiance	335.92	312.11	339.64	335.32
	PV power	3.29	2.973	3.123	3.086
Skewness	Irradiance	1.176	1.097	1.132	1.212
	PV power	1.07	0.95	1.01	1.05
Kurtosis	Irradiance	-0.096	0.100	-0.281	-0.157
	PV power	-0.43	-0.71	-0.56	-0.40

Method¹ represents the electrical image construction method in [8];

Method² represents the multi-channel construction method;

Method³ represents the single-channel construction method.

from low-temporal-resolution data. Thereafter, Fig. 7 illustrates the results of super-resolution reconstruction by different image construction methods. The first low-resolution image, the first high-resolution image, and the first reconstructed super-resolution image of the test set are shown in Fig. 7 (a ~ c). Compared with the low-resolution data-images, the super-resolution and high-resolution data-images are visually rich in high-resolution details and clear textures because the amount of data stored in such images are 16 times as much as that stored in low-resolution images. The super-resolution data-images store the reconstructed high-temporal-resolution data, and the high-resolution data-images store the real data. By measuring the difference between the reconstructed samples and real samples, we can evaluate the accuracy of image reconstruction method efficiently.

In Fig. 7 (a), although the pixels of super-resolution images are increased, the colors of them are messy, and the texture is different from high-resolution images, indicating that the electrical image construction

method does not have a high accuracy of image reconstruction. In Fig. 7 (b), the data-images constructed by the multi-channel method are encoded by many types of data. On the other hand, in Fig. 7 (c), the data-images constructed by the single-channel method are only encoded by one type of data. By contrast, it can be seen from Fig. 7 (b) and Fig. 7 (c) that, the texture of the super-resolution data-image is remarkably similar to that of the high-resolution data-image, indicating that the data-image construction method has a higher reconstruction quality.

To evaluate the quality of the reconstructed image, the PSNR and SSIM of the real samples and reconstructed samples are calculated in terms of formulas (11) and (12), and we take the average value of all test samples as the final statistical indicators. Table 1 lists the PSNR and SSIM of various image construction methods. Compared with the electrical image method, the proposed data-image construction method has a larger PSNR, which indicates that the results of the proposed data-image construction method are less distorted. Meanwhile, the SSIM of the proposed data-image construction method is relatively large, indicating that the proposed method enables the model to better extract the texture and tone of images. The results mean that the data-image construction method performs better on image reconstruction. In addition, compared with the data-image reconstructed by the multi-channel construction method, the PSNR, and SSIM of the data-image reconstructed by single-channel method are both larger, which means the single-channel method performs better on image reconstruction.

The data-images of the test set are converted into data in the form of time series, and the reconstructed curve on one day is compared with the corresponding real curve, as shown in Fig. 8. Among them, the left side is the reconstruction result of the electrical image construction method, and the right side is the reconstruction result of the single-channel construction method. Since the result of the multi-channel construction method is similar to that of the single-channel construction method, there are only the reconstruction results of the single-channel construction method in Fig. 8. It can be seen that the reconstructed curves obtained by the data-image construction method are almost similar to the real curves. Compared with the data-image construction method proposed in this paper, the reconstructed curves obtained by the method proposed in [8] do not correspond to the real curves on the timeline and lose some edge details. Hence, by encoding data into data-images, the distribution characteristics and edge details of PV generation data can be restored more effectively.

To evaluate the accuracy of the reconstructed data, the reconstructed data is compared with the corresponding real data, and the calculation results of various statistical indicators are shown in Table 2. In terms of Table 2, we have some discussions as follows:

- 1) In terms of MAE and RMSE statistics, the proposed method reduces the MAE and RMSE to about 1/2 of the original level, significantly improving the accuracy of the data reconstruction. At the same time, compared with the multi-channel method, the single-channel method has better data reconstruction performance and higher data reconstruction accuracy.
- 2) The R^2 of the data-image method is closer to one than that of the electrical image method, which indicates that the data reconstructed by the data-image can better represent the distribution characteristics of the PV generation than the data reconstructed by the electrical image proposed in [8]. In the same way, it can be seen that the single-channel method performs better than the multi-channel method.
- 3) In terms of indicators of Mean, Median and St.dev, the data reconstructed by the data-image method is always sufficiently close to the real data, while the data reconstructed by the electrical image proposed in [8] has larger errors than that of the data-image method. It shows that the data reconstructed from the data-image can better describe the statistical characteristics of the PV generation than the data obtained from the electrical image. From the perspective of these statistical indicators, the reconstruction effect of the single-channel method is similar to that of the multi-channel method.

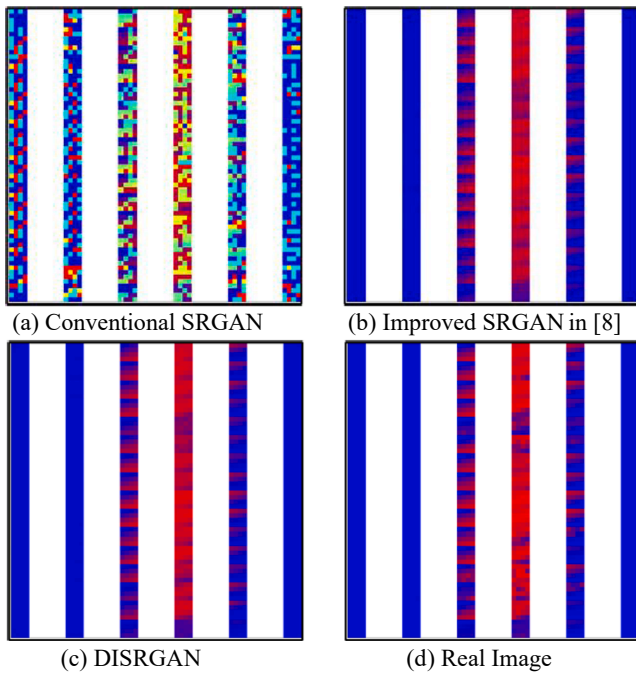


Fig. 9. Image reconstruction results of different SRGAN.

Table 3
Evaluation results of data reconstruction accuracy of different SRGAN model.

Statistic	Data type	Real	Model ¹	Model ²
MAE	Irradiance		60.10	50.33
	PV power		0.554	0.452
RMSE	Irradiance		106.23	94.94
	PV power		0.953	0.851
R ²	Irradiance		0.91	0.93
	PV power		0.91	0.93
Mean	Irradiance	247.20	251.28	248.48
	PV power	2.299	2.285	2.302
Median	Irradiance	0.00	36.42	26.36
	PV power	-0.019	0.215	0.185
St.dev	Irradiance	335.92	338.25	335.32
	PV power	3.29	3.23	3.086
Skewness	Irradiance	1.176	1.131	1.212
	PV power	1.07	1.119	1.05
Kurtosis	Irradiance	-0.096	-0.008	-0.157
	PV power	-0.43	-0.231	-0.40

Model¹ represents the conventional SRGAN model;

Model² represents the DISRGAN model.

Table 4
Training time of different SRGAN model.

SRGAN models	Irradiance Data	PV power Data
SRGAN in [8]	2312.78 s	2317.74 s
DISRGAN	995.95 s	1008.99 s

4) Concerning skewness and kurtosis indicators, the data reconstructed by the data-image method and the electrical image method proposed in [8] both deviate from the real data to some extent, and the errors of our method are always smaller than those of the method in [8]. It shows that the data reconstructed by the data-image method can better reflect the real skewness and kurtosis properties of PV generation data than the data reconstructed by the electrical image method. Similarly, it can be observed that the single-channel method performs better than the multi-channel method.

In this numerical test, the data-image construction method has a good performance with less prior data, which demonstrates that the seq2point mapping algorithm establishes the correlation between high-temporal-resolution and low-temporal-resolution PV generation data. Meanwhile, for the PV generation data, the binary image is adopted to effectively fix the pixel coordinates for storing data, enhancing the capability of DISRGAN model to extract data characteristics. Hence, the accuracy of data reconstruction can be improved by the data-image construction method.

5.4. Comparison between different SRGAN models

In this subsection, we use the single-channel construction method to encode data into data-images. We compare the performance of the proposed DISRGAN model with the conventional SRGAN model in [26] and the improved SRGAN model proposed in [8].

The irradiance data is taken for the super-resolution image reconstruction, and the reconstructed data-images are shown in Fig. 9. Compared with Fig. 9 (d), the color of Fig. 9 (a) is disordered, indicating that the reconstructed data-image obtained by the conventional SRGAN model fails to effectively recover the characteristic of the high-temporal-resolution data. By contrast, the texture of Fig. 9 (b) and Fig. 9 (c) are similar to that of Fig. 9 (d) from the perspective of vision.

Furthermore, to evaluate the performance enhancements of the proposed model, the evaluation results of the data reconstructed by the DISRGAN model are compared with those of the conventional SRGAN model, as shown in Table 3. It is clear that, except for the St.dev indicator, the performance of the proposed model is better than that of the conventional SRGAN model. The main reason is that the traditional JS distance used by the conventional loss function results in gradient disappearance and gradient instability in the training process. Consequently, the conventional SRGAN model is unable to extract enough data characteristics for reconstructing data effectively.

In addition to reconstruction accuracy, the model training time is also an important parameter in super-resolution reconstruction. Table 4 shows the training time of different SRGAN models required. Compared with the results of the improved SRGAN model proposed in [8], the training time of the DISRGAN model can be effectively reduced.

Due to that the existing SRGAN models have many different parameters, they need a long training process to reach the convergence state. By modifying the loss function and architecture, the proposed DISRGAN model is developed to speed up the training without decreasing the accuracy of data reconstruction.

6. Conclusion

In this paper, we propose a novel SRGAN-based method to reconstruct the high-temporal-resolution PV generation data from low-temporal-resolution data. Our proposed method mainly involves two parts: the data-image construction, the DISRGAN model design and training. At first, by encoding PV generation data into the proposed data-image, the data-image captures the data characteristics to improve the reconstruction accuracy. Thereafter, the DISRGAN model is developed to reduce the training time significantly without compromising accuracy. Finally, a general framework, which mainly consists of data-image and the DISRGAN model, is proposed for PV generation data reconstruction. The proposed method is tested on the dataset from the State Grid Corporation of China. The tests demonstrate the effectiveness of the proposed method.

By using our method, the quality of PV generation data will be improved, and the high-quality data can be utilized for various advanced data analysis methods to overcome the challenges caused by high PV penetration. In future work, we will test the proposed method on relatively higher temporal-resolution data, and focus on how to further improve the reconstruction accuracy.

CRediT authorship contribution statement

Chengsheng Zhang: Methodology, Software, Formal analysis, Data curation, Writing - original draft. **Zhenguo Shao:** Conceptualization, Writing - review & editing, Resources, Project administration, Funding acquisition, Supervision. **Changxu Jiang:** Conceptualization, Visualization, Methodology, Writing - review & editing. **Feixiong Chen:** Conceptualization, Validation, Methodology, Writing - review & editing.

Declaration of Competing Interest

The authors declare that they have no known competing financial interests or personal relationships that could have appeared to influence the work reported in this paper.

Acknowledgement

This work was supported in part by the National Natural Science Foundation of China (51777035), the Key Project of Natural Science Foundation of Fujian Province (2020J02028), and the Science and Technology Planning Project of Fuzhou (2020-PT-143).

Special thanks should go to State Power Rixin Technology Company Limited which provides the PV dataset from a photovoltaic power station.

References

- [1] Fang X, Misra S, Xue G, et al. Smart grid — the new and improved power grid: a survey. *IEEE Commun Surv Tutorials* 2012;14(4):944–80. <https://doi.org/10.1109/SURV.2011.101911.00087>.
- [2] Shaker H, Zareipour H, Wood D. Estimating power generation of invisible solar sites using publicly available data. *IEEE Trans Smart Grid* 2016;7(5):2456–65. <https://doi.org/10.1109/TSG.2016.2533164>.
- [3] Yang B, Wang J, Zhang X, et al. Comprehensive overview of meta-heuristic algorithm applications on PV cell parameter identification. *Energy Convers Manage* 2020;208. <https://doi.org/10.1016/j.enconman.2020.112595>.
- [4] Yang B, Wang J, Chen Y, et al. Optimal sizing and placement of energy storage system in power grids: A state-of-the-art one-stop handbook. *J Storage Mater* 2020;32. <https://doi.org/10.1016/j.est.2020.101814>.
- [5] Wang Y, Chen Q, Hong T, et al. Review of Smart Meter Data Analytics: Applications, Methodologies, and Challenges. *IEEE Trans Smart Grid* 2019;10(3):3125–48. <https://doi.org/10.1109/TSG.2018.2818167>.
- [6] Wang Y, Yan J, Yang Z, et al. Optimizing GIS partial discharge pattern recognition in the ubiquitous power internet of things context: A MixNet deep learning model. *Int J Electr Power Energy Syst* 2021;125. <https://doi.org/10.1016/j.ijepes.2020.106484>.
- [7] Alam SMS, Natarajan B, Pahwa A. Distribution grid state estimation from compressed measurements. *IEEE Trans Smart Grid* 2014;5(4):1631–42. <https://doi.org/10.1109/TSG.2013.2296534>.
- [8] Li F, Lin D, Yu T. Improved generative adversarial network based super resolution reconstruction for low frequency measurement of smart grid. *IEEE Access* 2020;8:85257–70. <https://doi.org/10.1109/ACCESS.2020.2992836>.
- [9] Krstulovic J, Miranda V, Pereira J. Reconstructing missing data in state estimation with autoencoders. *IEEE Trans Power Syst* 2012;27(2):604–11. <https://doi.org/10.1109/TPWRS.2011.2174810>.
- [10] Zhang F, Cheng L, Li X, et al. Application of a real-time data compression and adapted protocol technique for WAMS. *IEEE Trans Power Syst* 2015;30(2):653–62. <https://doi.org/10.1109/TPWRS.2014.2329092>.
- [11] Yang Z, Liu H, Bi T, et al. An adaptive PMU missing data recovery method. *Int J Electr Power Energy Syst* 2020;116. <https://doi.org/10.1016/j.ijepes.2020.106484>.
- [12] Tan B, Yang J, Zhou T, et al. Spatial-temporal adaptive transient stability assessment for power system under missing data. *Int J Electr Power Energy Syst* 2020;123. <https://doi.org/10.1016/j.ijepes.2020.106237>.
- [13] Li K, Yang S, Dong R, et al. Survey of single image super-resolution reconstruction. *IET Image Process* 2020;14(11):2273–90. <https://doi.org/10.1049/iet-ipr.2019.1438>.
- [14] Liu J, Gan Z, Zhu X. Directional bicubic interpolation - a new method of image super-resolution. In: 3rd Int. Conf. on Multimedia Technology (ICMT-13), Guangzhou, People's Republic of China, 2013, 463–470. <https://doi.org/10.2991/icmt-13.2013.57>.
- [15] Kumar G, Singh K. Image super resolution on the basis of DWT and bicubic interpolation. *Spectrochim Acta, Part B* 2013;89(89):84–92. <https://doi.org/10.1016/j.sab.2013.08.011>.
- [16] Yu L, Cao S, He J, et al. Single-image super-resolution based on regularization with stationary gradient fidelity. In: 10th Int. Congress on Image and Signal Processing, BioMedical Engineering and Informatics (CISP-BMEI), Shanghai, People's Republic of China 2017. p. 1–5.
- [17] Chang K, Ding PLK, Li B. Single image super resolution using joint regularization. *IEEE Signal Proc Lett* 2018;25(4):596–600. <https://doi.org/10.1109/LSP.2018.2815003>.
- [18] Dong C, Loy CC, He K, et al. Learning a deep convolutional network for image super-resolution. In: European Conf. on Computer Vision (ECCV2014), Zurich, Switzerland 2014. p. 184–99. DOI: 10.1007/978-3-319-10593-2_13.
- [19] Han W, Chang S, Liu D, et al. Image super-resolution via dual-state recurrent networks. In: Proc. IEEE Int. Conf. on Computer Vision and Pattern Recognition. (CVPR2018), Salt Lake City, UT, USA; 2018. p. 1654–1663. DOI: 10.1109/CVPR.2018.00178.
- [20] Zhang Y, Tian Y, Kong Y, et al. Residual dense network for image super-resolution. In: Proc. IEEE Int. Conf. on Computer Vision and Pattern Recognition (CVPR2018), Salt Lake City, UT, USA; 2018. p. 2472–81. DOI: 10.1109/CVPR.2018.00262.
- [21] Ahn N, Kang B, Sohn KA. Fast, accurate, and lightweight super-resolution with cascading residual network. In: European Conf. on Computer Vision (ECCV2018), Munich, Germany; 2018. p. 252–268.
- [22] Zhang Y, Li K, Li K, et al. Image super-resolution using very deep residual channel attention networks. In: European Conf. on Computer Vision (ECCV2018), Munich, Germany; 2018. p. 286–301.
- [23] Liang G, Liu G, Zhao J, et al. Super Resolution Perception for Improving Data Completeness in Smart Grid State Estimation. *Engineering* 2020;6(7):789–800. <https://doi.org/10.1016/j.eng.2020.06.006>.
- [24] Liu G, Gu J, Zhao J, et al. Super Resolution Perception for Smart Meter Data. *Inf Sci* 2020;526:263–73. <https://doi.org/10.1016/j.ins.2020.03.088>.
- [25] Kim J, Lee J K and Lee K M. Accurate Image Super-Resolution Using Very Deep Convolutional Networks. In: Proc. IEEE Int. Conf. on Computer Vision and Pattern Recognition (CVPR2016), Las Vegas, NV; 2016. p. 1646–1654. DOI: 10.1109/CVPR.2016.182.
- [26] Ledig C, Theis L, Huszar F, et al. Photo-realistic single image super-resolution using a generative adversarial network. In: Proc. IEEE Int. Conf. on Computer Vision and Pattern Recognition (CVPR2017), Venice, Italy; 2017. p. 4681–4690. DOI: 10.1109/CVPR.2017.19.
- [27] Goodfellow IJ, Pouget-Abadie J, Mirza M, et al. Generative adversarial nets. In: Proc. Adv. Neural Inf. Proces. Syst (NIPS 2014), Montreal, QC, Canada 2014;3:2672–2680.
- [28] Ren C, Xu Y. A fully data-driven method based on generative adversarial networks for power system dynamic security assessment with missing data. *IEEE Trans Power Syst* 2019;34(6):5044–52. <https://doi.org/10.1109/TPWRS.2019.2922671>.
- [29] Chen Y, Wang Y, Kirschen DS, et al. Model-free renewable scenario generation using generative adversarial networks. *IEEE Trans Power Syst* 2018;33(3):3265–75. <https://doi.org/10.1109/TPWRS.2018.2794541>.
- [30] Zhang Y, Ai Q, Xiao F, et al. Typical wind power scenario generation for multiple wind farms using conditional improved Wasserstein generative adversarial network. *Int J Electr Power Energy Syst* 2020;114. <https://doi.org/10.1016/j.ijepes.2019.105388>.
- [31] Zhou B, Duan H, Wu Q, et al. Short-term prediction of wind power and its ramp events based on semi-supervised generative adversarial network. *Int J Electr Power Energy Syst* 2021;125. <https://doi.org/10.1016/j.ijepes.2020.106411>.
- [32] Yuan Y, Dehghanpour K, Bu F, et al. Outage detection in partially observable distribution systems using smart meters and generative adversarial networks. *IEEE Trans Smart Grid* 2020;11(6):5418–30. <https://doi.org/10.1109/TSG.2020.3008770>.
- [33] D'Incecco M, Squartini S, Zhong M. Transfer learning for non-intrusive load monitoring. *IEEE Trans Smart Grid* 2020;11(2):1419–29. <https://doi.org/10.1109/TSG.2019.2938068>.
- [34] Arjovsky M, Chintala S, Bottou L. Wasserstein GAN. *ArXiv*, ID: 1701.07875v3. 2017;1–32.
- [35] He K, Zhang X, Ren S, et al. Deep residual learning for image recognition. In: Proc. IEEE Int. Conf. on Computer Vision and Pattern Recognition (CVPR2016), Las Vegas, NV, USA 2016. p. 770–778. DOI: 10.1109/CVPR.2016.90.
- [36] Shi W, Caballero J, Huszar F, et al. Real-time single image and video super-resolution using an efficient sub-pixel convolutional neural network. In: Proc. IEEE Int. Conf. on Computer Vision and Pattern Recognition (CVPR2016), Las Vegas, NV, USA; 2016. p. 1874–1883. DOI: 10.1109/CVPR.2016.207.
- [37] He K, Zhang X, Ren S, et al. Delving deep into rectifiers: surpassing human-level performance on ImageNet classification. In: Proc. IEEE Int. Conf. on Computer Vision (ICCV2015), Santiago, USA; 2015. p. 1026–1034. DOI: 10.1109/ICCV.2015.123.
- [38] Krizhevsky A, Sutskever I, Hinton G. ImageNet classification with deep convolutional neural networks. In: Proc. Adv. Neural Inf. Process. Syst. (NIPS), Lake Tahoe, America; 2012. p. 1097–1105. DOI: 10.1145/3065386.
- [39] Xu B, Wang N, Chen T, et al. Empirical evaluation of rectified activations in convolutional network. *ArXiv*, ID: 1505.00853v2 2015. p. 1–5.
- [40] PyTorch, from GitHub, accessed Oct. 2017, available at <https://github.com/pytorch>.
- [41] Welstead ST. *Fractal and Wavelet Image Compression Techniques*. USA: Society of Photo-Optical Instrumentation Engineers (SPIE); 1999.
- [42] Wang Z, Bovik AC, Sheikh HR, et al. Image quality assessment: from error visibility to structural similarity. *IEEE Trans Image Process* 2004;13(4):600–12. <https://doi.org/10.1109/TIP.2003.819861>.